

# Magnetic Superexchange Induced Quantum Phase Transition in Cr<sub>2</sub>B<sub>2</sub> MBene

Shucheng Xing, Jian Zhou,\* Bikun Zhang, and Zhimei Sun\*



Cite This: *J. Phys. Chem. C* 2022, 126, 14275–14282



Read Online

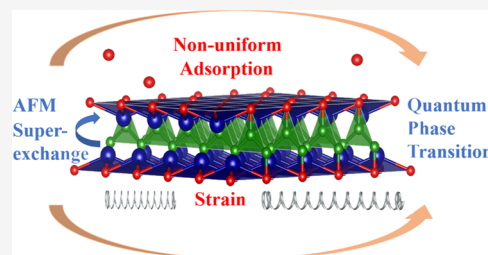
ACCESS |

Metrics & More

Article Recommendations

Supporting Information

**ABSTRACT:** Stable long-range magnetic order in low-dimensional semiconductors up to room temperature has long been the pursuit of researchers for their potential applications in the field of spintronic and memory devices. However it is a great challenge to achieve magnetic phase transition together with a controllable band structure in two-dimensional magnetic materials simultaneously. Through fully terminated oxygen group adsorption, the transformation from ferromagnetic metal to antiferromagnetic semiconductor with a high Néel temperature (425 K) has been achieved in Cr<sub>2</sub>B<sub>2</sub> MBene, which is attributed to superexchange interaction between the interlayer magnetic chromium (Cr) atoms. Furthermore, exotic quantum phase transition between two different antiferromagnetic states of Cr<sub>2</sub>B<sub>2</sub>O<sub>2</sub>, together with the transition from semiconductor to metal, is observed when applying compressive strain. Interestingly, ferromagnetic half-metal and ferromagnetic semiconductor states are achieved by nonuniform oxygen group adsorption, resulting from electrical potential difference between the Cr atomic layers and thus built-in electric field. Our results reveal the origin of magnetic phase transition in Cr<sub>2</sub>B<sub>2</sub> MBene and offer a new avenue to obtain magnetic multifunctional materials for spintronic devices.



## INTRODUCTION

Spin-based electronics, utilizing both the charge and spin freedom of electron, can offer an ideal platform for information technology.<sup>1,2</sup> Controllable tuning of electrical and magnetic properties for spintronic applications, manifested in full manipulation of charge and spin at the quantum level, has led to tremendous advances in fundamental condensed matter research and microelectronic applications.<sup>1</sup> Spin manipulation mainly manifests in the regulation of spin coupling. Strong adjacent spin coupling interaction with considerable magnetic anisotropy may result in the ordered arrangement of atomic magnetic moments, which could resist the thermal fluctuations under transition temperature.<sup>3</sup>

Nevertheless, most materials, especially low-dimensional materials, have weak magnetic exchange interaction without long-range magnetic order at room temperature.<sup>4,5</sup> To strengthen the coupling interaction, several methods that can break the symmetry of the material emerged, such as surface decoration,<sup>6–8</sup> strain,<sup>9–11</sup> or the application of electric fields.<sup>12–14</sup> In these processes, the changed coupling interaction also could induce the magnetic phase transition of the material, leading to favorable functionalities, such as giant magnetocaloric effect<sup>15</sup> and colossal magnetoresistance.<sup>16</sup> When the external regulations are introduced, the varied electron correlations affect the electronic states, including the localization of the electrons.<sup>17</sup> The degree of localization of the electrons is closely related to the energy levels near the Fermi surface, which in turn affects the electrical properties of the material.<sup>18</sup> Therefore, finding suitable methods and materials

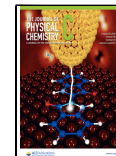
to realize the simultaneous control of charge and spin is critical for the modulation of electrical and magnetic properties for spintronic devices.

Two-dimensional (2D) materials with a quantum confinement effect of electron exhibit great spin-dependent properties, such as ultralong spin relaxation time,<sup>19</sup> spin diffusion length,<sup>20</sup> and Rashba spin-orbit coupling.<sup>21</sup> Simultaneously, plenteous control methods applied in 2D materials benefit from the huge specific surface area and excellent mechanical properties.<sup>22</sup> Some 2D materials with magnetic metal atoms have been widely studied, which are reported with high transition temperature, leading to the potential application for spintronic devices.<sup>23–26</sup> A fast-growing family of 2D materials, known as 2D transition-metal borides (MBenes) were introduced, where M is a transition metal and B is boron.<sup>27,28</sup> Most group-functionalized MBenes were demonstrated to exhibit metallicity, showing excellent performance in lithium/sodium-ion battery electrodes<sup>27,29</sup> and electrocatalyst,<sup>30,31</sup> while rare reports already predicted magnetic semiconductivity in MBenes. Meanwhile, MBenes are great candidates for low-dimensional magnetic materials owing to the coupling with the

Received: June 6, 2022

Revised: July 24, 2022

Published: August 11, 2022



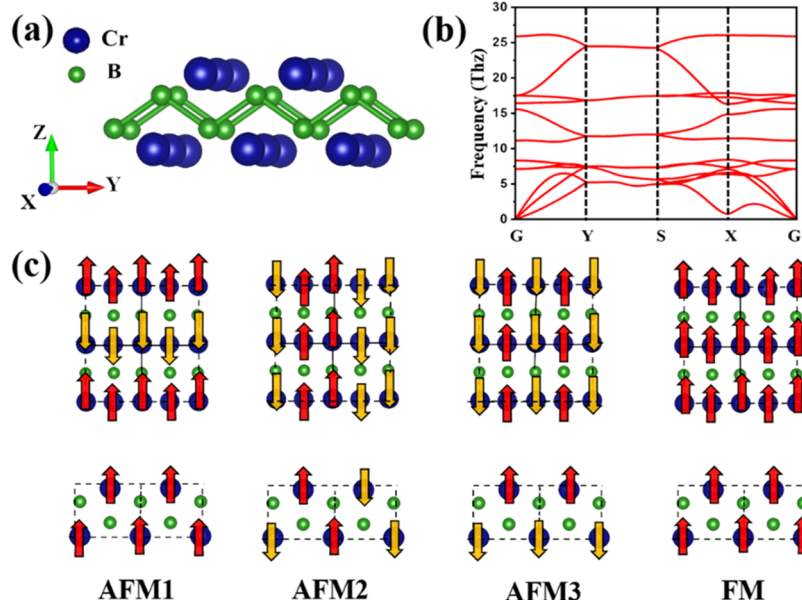


**Figure 1.** (a) Structure of Cr<sub>2</sub>B<sub>2</sub> ( blue and green spheres represent Cr and B atoms, respectively), (b) phonon dispersion of Cr<sub>2</sub>B<sub>2</sub>, and (c) four different magnetic ground states of Cr<sub>2</sub>B<sub>2</sub> ( up and down arrows indicate spin-up and spin-down, respectively).

unpaired *d* electrons in transition-metal elements.<sup>32,33</sup> The pristine Cr<sub>2</sub>B<sub>2</sub> MBene is a typical magnetic metal whose magnetic properties have been thoroughly investigated in previous study.<sup>34</sup> Nevertheless, the functional group adsorption is usually occurred during the experimental preparation process, which would have great impact on the localization and spin correlation of electrons.

In this work, the localization and spin correlation of electrons are regulated by adsorbing the oxygen functional group, leading to the transition from ferromagnetic (FM) metal to antiferromagnetic (AFM) insulator in MBene Cr<sub>2</sub>B<sub>2</sub>. The AFM order of Cr<sub>2</sub>B<sub>2</sub>O<sub>2</sub> is arising from interlayer superexchange interaction, while the intralayer coupling shows ferromagnetism, which can resist the thermal fluctuation up to 425 K. Furthermore, the transition between two different antiferromagnetic states of Cr<sub>2</sub>B<sub>2</sub>O<sub>2</sub>, together with the transition from semiconductor to metal, is observed when applying compressive strain. The band gap of the Cr<sub>2</sub>B<sub>2</sub>O<sub>2</sub> semiconductor state and the phase transition temperature can be continuously regulated by both tensile and compressive stains. By nonuniform oxygen group adsorption, the electrical potential difference between the Cr atomic layers is introduced to create a built-in electric field. The ferromagnetic half-metal and ferromagnetic semiconductor are achieved, which offers a new avenue to design multifunctional spintronic devices.

## METHODS

Our calculations are performed in the framework of density functional theory as implemented in the Vienna ab initio simulation package (VASP).<sup>35</sup> The projector augmented wave (PAW) potential<sup>36</sup> is used with the plane-wave cutoff energy set as 500 eV. The system is modeled by a pristine or functionalized Cr<sub>2</sub>B<sub>2</sub> MBene single layer and a vacuum region more than 20 Å to avoid interaction between neighboring slabs. The Brillouin zone is integrated with 8 × 8 × 1 *k*-point mesh. In GGA + *U* calculations, the Hubbard *U* is set to 4 eV. The value of *U* was carefully tested by comparing the

calculation results and experimental results<sup>37</sup> of the lattice constants and cell volumes based on the previous works.<sup>38,39</sup>

The phonon spectra are calculated using the density functional perturbation theory (DFPT) method as implemented in the PHONOPY code<sup>40</sup> combined with VASP. The Heyd–Scuseria–Ernzerhof (HSE) screened coulombic hybrid density functional<sup>41</sup> is used to describe the electron correlation effects in the band structure and density of states calculations. All of the structures are fully relaxed until the remaining force acting on each atom is less than 0.01 eV/Å. The adsorption energy is calculated by the following formula<sup>42</sup>

$$E_{\text{ads}} = \frac{E_{\text{total}} - E_{\text{slab}} - n \times E_{\text{adsorbate}}}{n}$$

where *E*<sub>total</sub> is the energy after system adsorption, *E*<sub>slab</sub> is the energy of slab, *E*<sub>adsorbate</sub> is the energy of adsorbed functional group at its optimized geometry, and *n* represents the number of adsorbate groups in the simulation cell.

The magnetic properties of the material are investigated with the Heisenberg method, and the exchange constants are calculated using the Green's function method by the TB2J code<sup>43</sup> interfaced with OpenMX.<sup>44</sup> The magnetic exchange coupling constants are derived by comparing the energy change due to a small spin rotation between the Heisenberg model and Green's-function energy expression, utilizing the local force theorem.<sup>45</sup> The Heisenberg exchange coupling constant *J* for local spin vectors of unit length can be obtained as the imaginary part of an integral over the trace of products of the Green's functions for  $\alpha$  and  $\beta$  spins and so-called on-site potentials  $\hat{V}_A$  and  $\hat{V}_B$  of the two magnetic sites.

$$J_{\text{Green}}^{\text{unit}}(F) = -\frac{1}{4\pi} \text{Im} \int_{-\infty}^{\epsilon_F} d\epsilon \text{Tr}[\hat{V}_A \hat{G}^\alpha \hat{V}_B \hat{G}^\beta]$$

The on-site potentials can be expressed as the difference between the Coulomb potentials for  $\alpha$  and  $\beta$  electrons,  $\hat{U}_A^\alpha$  and  $\hat{U}_A^\beta$ , respectively.

$$\hat{V}_A = \hat{U}_A^\alpha - \hat{U}_A^\beta$$

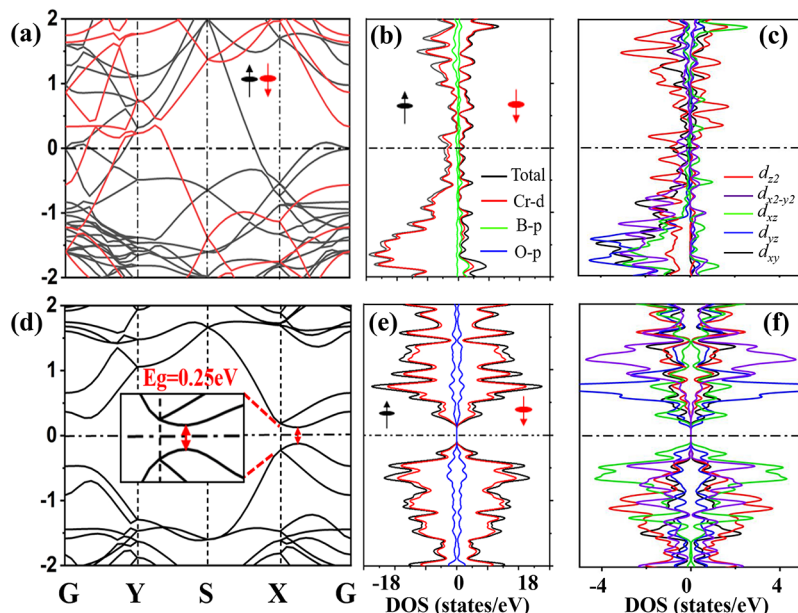


**Figure 2.** Band structures and projected density of states of Cr<sub>2</sub>B<sub>2</sub> (a–c) and Cr<sub>2</sub>B<sub>2</sub>O<sub>2</sub> (d–f) (up and down arrows indicate spin-up and spin-down, respectively).

All of the fitted magnetic exchange constants are used to do spin dynamics with the VAMPIRE code.<sup>46</sup> For calculating the phase transition Néel temperature and temperature-dependent magnetization, the Landau–Lifshitz–Gilbert (LLG) approach is adopted. Other calculation details are listed in the Supporting Information.

## RESULTS AND DISCUSSION

The crystal structure of Cr<sub>2</sub>B<sub>2</sub> MBene is depicted in Figure 1a. It is an orthogonal lattice structure where each chromium atom bonds with four surrounding boron atoms in the same atomic layer. The phonon dispersion shown in Figure 1b with no negative frequency verifies that Cr<sub>2</sub>B<sub>2</sub> is dynamically stable. 2 × 2 × 1 supercell of Cr<sub>2</sub>B<sub>2</sub>, where eight Cr atoms are included, is constructed to consider the magnetic coupling between the Cr atoms. Four different magnetic ground states, AFM1, AFM2, AFM3, and FM, are shown in Figure 1c. The energy differences between AFM and FM states ( $\Delta_{\text{AFM1-FM}} = 0.11$  eV/cell,  $\Delta_{\text{AFM2-FM}} = 0.15$  eV/cell, and  $\Delta_{\text{AFM3-FM}} = 0.18$  eV/cell) show that Cr<sub>2</sub>B<sub>2</sub> forms ferromagnetic order, which is consistent with the previous work,<sup>31</sup> when using the same Hubbard  $U$ . It is noted that the Hubbard  $U$  should be carefully considered, as the calculation of magnetic and electronic properties is closely related to the value of Hubbard  $U$ .<sup>34</sup> The electronic structure of Cr<sub>2</sub>B<sub>2</sub> can then be achieved when the magnetic ground state of Cr<sub>2</sub>B<sub>2</sub> has been determined. The calculated spin-polarized band structure and atom- and orbital-projected density of states (Figure 2a–c) further reveal that the magnetism in the Cr<sub>2</sub>B<sub>2</sub> monolayer is mainly contributed by 3d orbitals of Cr atoms. The broad and low peaks in the density of states plot indicate that the 3d electrons of Cr are itinerant. Inhomogeneity of orbital contributions from different spin channels reflects ferromagnetism in the density of states, where  $d_{x2-y2}$  and  $d_{yz}$  orbitals show nearly in the spin-up channel. Highly delocalized electrons in Cr<sub>2</sub>B<sub>2</sub> lead to itinerant ferromagnetism according to the stoner model, which is consistent with previous reports.<sup>47</sup>

During the synthesis of MBenes, A is etched from MAB phases (where A is a main group element) in the hydrofluoric acid or a solution of lithium fluoride, which will easily lead to the termination of the MBenes surfaces by oxygen or hydroxide groups.<sup>48</sup> Among all possible adsorbed functional groups, the adsorption of oxygen functional group is the easiest to form when exposed to air. Furthermore, functionalization as a prevailing control method affects the localized properties of electrons by bonding and changes the magnetic exchange interactions between magnetic atoms. Therefore, we have also studied the electronic and magnetic properties of oxygen-functionalized Cr<sub>2</sub>B<sub>2</sub>. The ultralow adsorption energy (−0.29 eV/atom), compared with widely investigated two-dimensional transition-metal carbides (Ti<sub>2</sub>C: −0.12 eV/atom and Nb<sub>2</sub>C: −0.11 eV/atom),<sup>49</sup> indicates that the functional group will be easily adsorbed on the surface of Cr<sub>2</sub>B<sub>2</sub> MBene. The spin-orbit coupling (SOC) effect on Cr<sub>2</sub>B<sub>2</sub>O<sub>2</sub> has been considered. Little influence of SOC on the electronic structures is manifested from the comparison of the band structure with/without considering the SOC shown in Figure S1. Therefore, the impacts of SOC are not discussed in the subsequent discussion.

The spin-polarized band structure and atom- and orbital-projected density of states (Figure 2d–f) are calculated for Cr<sub>2</sub>B<sub>2</sub>O<sub>2</sub> as well. The intriguing antiferromagnetic semiconductor characteristic of Cr<sub>2</sub>B<sub>2</sub>O<sub>2</sub> is found, which can be broadly used for terahertz information technologies or artificial neural networks.<sup>2,50</sup> The magnetism originates from the d electrons of Cr<sub>2</sub>B<sub>2</sub>O<sub>2</sub> as well, while the narrow and high peaks of density of states indicate that the d electrons are highly localized, suggesting the reduced possibility of direct coupling d orbitals. Hereafter, the magnetism in the system mainly originates from the superexchange interactions between the magnetic Cr atoms. To discuss the magnetic interactions between the Cr atoms in Cr<sub>2</sub>B<sub>2</sub>O<sub>2</sub>, the Heisenberg model is introduced, which is particularly suitable for describing the magnetic exchange system of the local electronic model. The

highly localized  $d$  electrons are well described by the Heisenberg model

$$H = - \sum_{i,j} J_{ij} S_i S_j - \sum_{k,l} J_{kl} S_k S_l - K_z \sum_l (S_l^z)^2$$

where  $J$  is the coupling constant,  $S$  is the net spin of Cr, and  $K$  represents uniaxial magnetic anisotropy along the  $z$  direction.

Considering the structure of  $\text{Cr}_2\text{B}_2\text{O}_2$  in Figure 3a, one layer of boron atoms is sandwiched between two layers of chromium

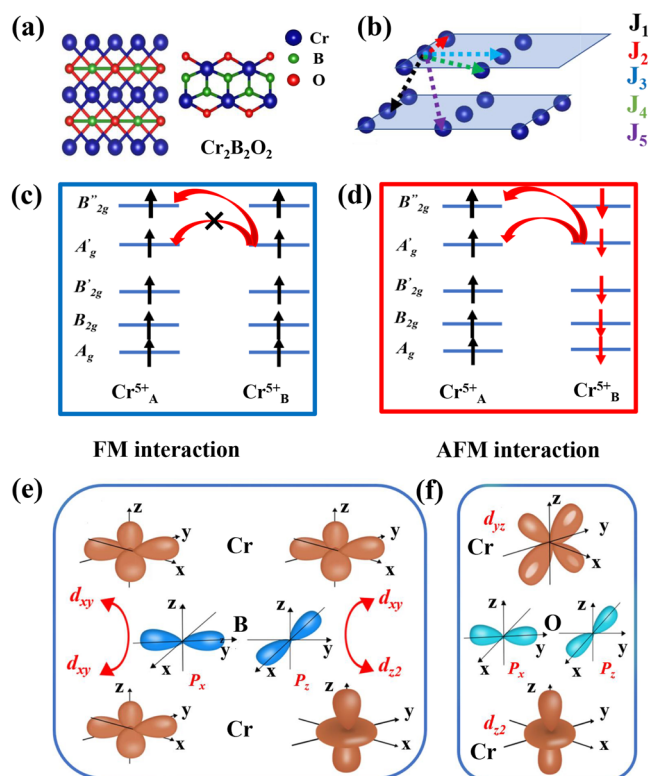


**Figure 3.** (a) Structure of  $\text{Cr}_2\text{B}_2\text{O}_2$ . (b) Exchange interactions of interlayer and intralayer. (c, d) Schematic diagrams of FM interaction and AFM interaction in  $\text{Cr}_2\text{B}_2\text{O}_2$ , respectively ( $\text{Cr}_{\text{A}}^{5+}$  and  $\text{Cr}_{\text{B}}^{5+}$  represent two different Cr ions in virtual exchange). Orbital resolved exchange interactions between interlayer and intralayer (e, f), respectively (orbitals of the Cr, B, and O atoms are shown in brown, blue, and green schematic diagram; red characters represent orbitals belonging to corresponding atoms).

atoms. Both interlayer and intralayer magnetic exchanges determine the magnetic ground state. The schematic diagram of exchange interactions between the nearest-neighbor and next-nearest-neighbor Cr atoms for interlayer ( $J_1, J_5$ )/intralayer ( $J_2, J_3, J_4$ ) is considered, which is depicted in Figure 3b.  $\text{Cr}_2\text{B}_2\text{O}_2$  is a tetrahedrally coordinated system with  $D_{2h}$  point symmetry, the fivefold degenerated  $d$  electron energy level splits into five singlet states, namely,  $A_g, B_{2g}, B'_{2g}, A'_g$  and  $B''_{2g}$  due to the tetrahedral crystal effect. These five states correspond to the five orbitals of the  $d$  electron:  $d_{xy}, d_{yz}, d_{zx}, d_{x^2-y^2}$ , and  $d_{z^2}$ . Figure 3c,d shows a schematic exchange mechanism of FM and AFM coupling for  $\text{Cr}_2\text{B}_2\text{O}_2$ . The virtual hopping from different orbitals between two chromium atoms would happen, leading to particular magnetic order. For example, virtual hopping of the form  $A'_g-A'_g$  is prohibited in FM exchange, whereas this is allowed in AFM exchange, according to the Pauli exclusion principle. Using the

Heisenberg model and Green function method, five magnetic exchange constants are calculated ( $J_1 = -22.19, J_2 = 9.09, J_3 = -1.26, J_4 = 11.96, J_5 = -13.79$  meV; the positive and negative  $J$  values indicate the ferromagnetic and antiferromagnetic exchange constants, respectively). The results show that the antiferromagnetism of  $\text{Cr}_2\text{B}_2\text{O}_2$  mainly arises from the interlayer coupling of Cr atoms while the intralayer couplings result in ferromagnetic feature. From this perspective,  $\text{Cr}_2\text{B}_2\text{O}_2$  is analogous to stack two ferromagnetic layers with inverse spin orientations. Due to the localization of Cr electrons, superexchange interactions between two interlayer Cr sites, utilizing  $p$  electron of B as a bridge, are the origin of antiferromagnetism in  $\text{Cr}_2\text{B}_2\text{O}_2$ . The main contribution of interlayer switching originates from  $J_1$  interaction. When decomposing the Cr–Cr exchange interaction of  $J_1$  into orbitals, the  $d_{xy}-d_{xy}$  and  $d_{xy}-d_{z^2}$  hybridization between the  $p_x$  and  $p_z$  orbitals of boron mainly contributes to the antiferromagnetic exchange. The in-plane ferromagnetic coupling mainly arises from the  $d_{yz}-d_{z^2}$  superexchange interaction of Cr ions, utilizing  $p_x$  and  $p_z$  orbitals of oxygen as a bridge. The  $d_{xy}-d_{xy}$  virtual electron overlap between the  $p$  orbital is only permitted for electrons with different spin orientations, which eventually mainly contribute to the interlayer antiferromagnetism. The magnetic interactions between orbitals for interlayer and intralayer are depicted in Figure 3e,f, respectively. This conclusion is also consistent with the Goodenough–Kanamori–Anderson (GKA) rule that superexchange interactions are antiferromagnetic where the virtual electron transfer is between overlapping orbitals that are each half-filled.<sup>51,52</sup> In conclusion, the oxygen group adsorption in  $\text{Cr}_2\text{B}_2$  MBene contributes the delocalization-to-localization transition of  $d$  electrons owing to the strong chemical bonding. The interlayer superexchange interactions between localized  $d$  electron, utilizing B  $p$  electrons as a bridge, lead to the antiferromagnetism of  $\text{Cr}_2\text{B}_2\text{O}_2$ , while the intralayer interactions show ferromagnetic characteristics, utilizing O  $p$  electrons as a bridge.

Magnetic anisotropy is the critical factor for 2D magnetic materials as it prevents random spin reorientations induced by thermal fluctuations, which mainly depends on two elements: spin-orbit coupling and magnetostatic dipole–dipole interactions, contributing to the magnetocrystalline anisotropy and shape anisotropy, respectively.<sup>53</sup> The magnetic anisotropy energy (MAE) can be expressed as

$$E = E_0 + K_2 \sin^2 \theta + K_4 \sin^4 \theta$$

where  $K_2$  and  $K_4$  represent the magnetocrystalline anisotropy coefficients, determined by the magnetic force theorem and  $\theta$  is the angle between the normal axis and the direction of magnetization.<sup>54</sup> The values of  $K_2$  for  $xz$  and  $yz$  planes are 81 and  $48.9 \mu\text{eV}$  per Cr atom, respectively, extracted from the fitted line shown in Figure S2. The positive values of  $K_2$  indicate that both  $\text{MAE}_{xz}$  and  $\text{MAE}_{yz}$  give a preferred easy axis orientation. The Néel temperature of  $\text{Cr}_2\text{B}_2\text{O}_2$  is estimated by Monte Carlo simulation. The relationship between the normalized magnetic moment and temperature is depicted in Figure S3, where the Néel temperature is about 425 K. According to the simulation of Monte Carlo in Figure S3, the Néel temperature is slightly decreased when magnetic anisotropy is not considered. This suggests that the effect of MAE on the phase transition temperature of  $\text{Cr}_2\text{B}_2\text{O}_2$  is not significant.

Strain engineering is a promising route to modulate the electronic and magnetic properties of 2D materials. Here, we

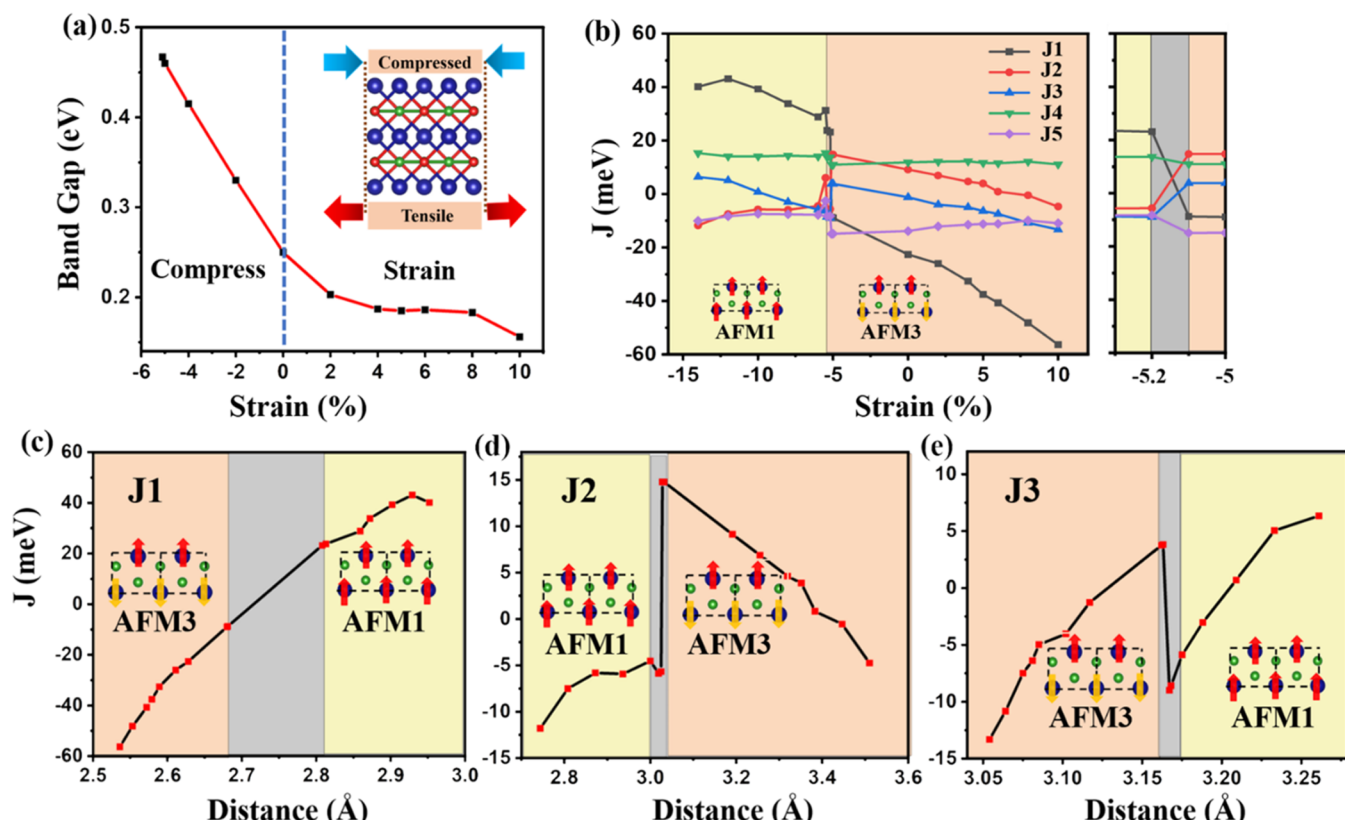


**Figure 4.** (a) Band gap versus strain along zigzag direction. (b) Magnetic exchange constants versus strain. (c–e). Magnetic exchange constants  $J_1$ ,  $J_2$ , and  $J_3$  versus distance between corresponding Cr atoms.

investigate the influences on the magnetic and electronic properties of fully adsorbed  $\text{Cr}_2\text{B}_2\text{O}_2$  by applying strain engineering. Uniaxial stress-strain curves along zigzag and armchair directions have been calculated to evaluate the deformation resistance of  $\text{Cr}_2\text{B}_2\text{O}_2$  shown in Figure S4. Here, the percentage of applied strain is defined as positive and negative values for tensile and compressive strains, respectively. The results show that  $\text{Cr}_2\text{B}_2\text{O}_2$  has good deformability up to 20% tensile strain and -10% compressed strain without structure damage. The magnetic ground states under various strains are first determined, and the results are listed in Tables S1 and S2, for applying strains along with zigzag and armchair directions, respectively. The calculated electronic band edges of 2D monolayer  $\text{Cr}_2\text{B}_2\text{O}_2$  under various strains with respect to vacuum are shown in Figure S5 and the band structures for different states are calculated subsequently as shown in Figures S6–S9. It is worth noting that the phase transition from the AFM3-semiconductor (0.47 eV band gap) to AFM1-metal occurs at -5.1% compressed strain along the zigzag direction. When applying strain along the zigzag direction up to 8% tensile strain, the system will show transition from direct band gap to indirect band gap semiconductor. Moreover, the phase transition from AFM3-semiconductor (0.3 eV band gap) to AFM2-metal can be achieved as well, at -8% compressed strain along armchair direction. Before the phase transition occurs, the system remains in the semiconducting state and the band gap can be continuously regulated, as shown in Figure 4a.

To understand this magnetic phase transition, magnetic exchange constants for different strains are calculated using the Green's function method, which are shown in Tables S3 and S4. When applying strain along the zigzag direction, the

exchange constants for different strains are plotted in Figure 4b. It is obvious that there is a mutation of  $J_1$ ,  $J_2$ , and  $J_3$  from -5.2% stain to -5.1% strain, which shows that the intralayer and interlayer coupling together leads to such a transition. The relations between interlayer exchange constants ( $J_1$ ,  $J_2$ , and  $J_3$ ) and interatomic distances are plotted in Figure 4c–e. Figure 4c shows that the mutation of  $J_1$  is accompanied by the huge variation of the distance between atoms when strain up to -5.1%. The orbital decomposed exchange constants are calculated to trace the origin of this transition. In the -5.1% strained system,  $d_{xy}-d_{xy}$  interlayer antiferromagnetic coupling in  $J_1$  is strengthened compared to -5.2% strained system. While between the intralayer coupling, the ferromagnetic coupling of the -5.1% strained system enhances for  $d_{yz}-d_{yz}$  coupling. When applying strain along the armchair direction, the phase transition also occurs mainly due to the change of interlayer superexchange constant  $J_1$  as well. Therefore, the strain will cause a great change in the magnetic exchange between inter/intralayers, which will eventually lead to a transition between different antiferromagnetic states. The phase transition temperature of  $\text{Cr}_2\text{B}_2\text{O}_2$  in antiferromagnetic state can be modulated by applying uniaxial strain, and the results are shown in Figures S10 and S11. For compressive strain, the Néel temperature increases slightly along both the zigzag and armchair directions. When the tensile strain is applied along the armchair direction, the Néel temperature is slightly reduced with increasing strain. Nevertheless, the Néel temperature does not change much when applying tensile strain along the zigzag direction. Therefore, small compressive strain can be applied to  $\text{Cr}_2\text{B}_2\text{O}_2$  to raise the Néel temperature.

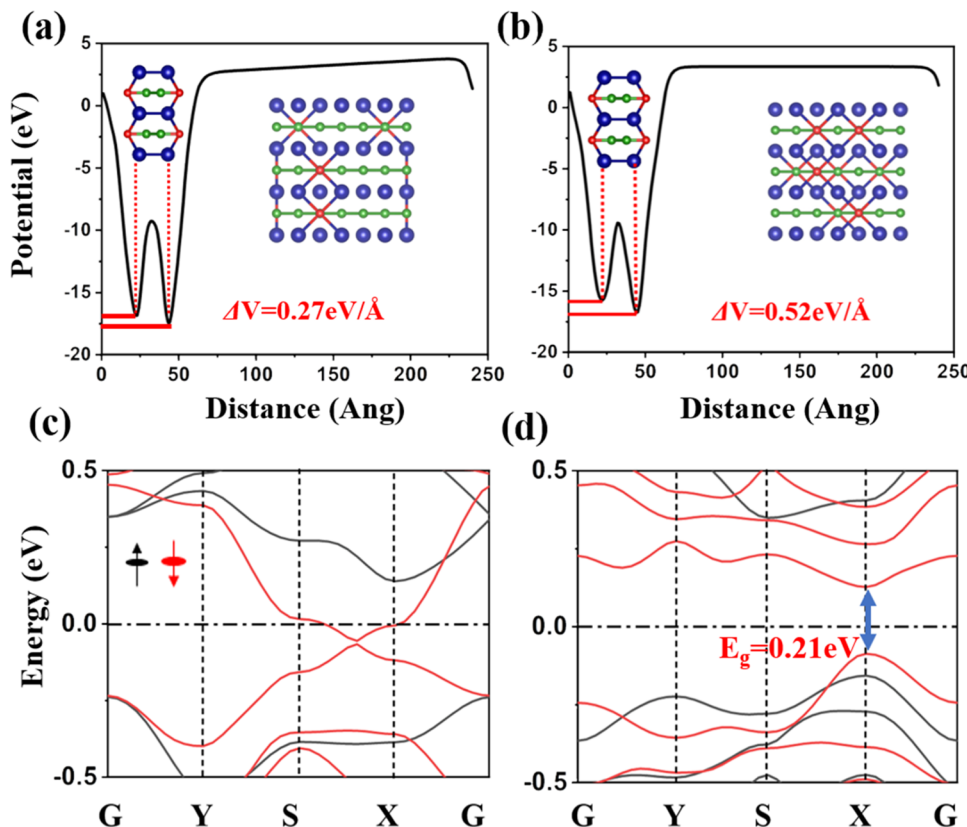


**Figure 5.** Adsorption structures and potential differences between chromium layer for 33.3% (a) and 44.4% (b) oxygen concentrations, respectively. Band structures of 33.3% (c) and 44.4% (d) oxygen concentrations, respectively.

The  $\text{Cr}_2\text{B}_2\text{O}_2$  MBene considered above is fully terminated by the oxygen functional group. While during the actual experimental preparation periods, the process of oxygen adsorption is continuous, and the adsorbed sites tend to be disordered.<sup>55</sup> Thus, considering the nonuniformity of oxygen adsorption is critical for evaluating the effects on magnetic and electronic properties. By calculating the energies of oxygen adsorption on the nearest and farthest neighbors of  $\text{Cr}_2\text{B}_2$ , we found that the energy of oxygen adsorption is lower when the distance is farther. The comparison of energies for these two structures is shown in Table S5 (type1 and type2 structures of 25% oxygen concentration). This indicates that when insufficient oxygen atoms are adsorbed, oxygen atoms tend to disperse and a disordered configuration would be obtained. Therefore, we selected several configurations for different concentrations of oxygen adsorption. Nine configurations with three concentrations of 25%, 50%, and 75% are shown in Figure S12. When the concentration exceeds 50%, the system of  $\text{Cr}_2\text{B}_2\text{O}_{2-x}$  still maintains the antiferromagnetic ground state, but at 25%, it exhibits ferromagnetism like  $\text{Cr}_2\text{B}_2$ . The results show that the magnetic ground state is highly related to the concentration of oxygen. It suggests that there is a transition concentration where a ferromagnetic-to-antiferromagnetic transition occurs between 25% and 50% oxygen adsorption concentrations. Not only the adsorption concentration but also the specific adsorption configuration affects the ground state of the system. It is highly noticed that the asymmetrical adsorption on both sides can introduce the potential difference between the layers, break the space reversal symmetry, and lead to a built-in electric field. The oxygen adsorption concentrations of 33.3% and 44.4% with a  $3 \times 3$

1 supercell have been considered. We construct a potential difference by adatoms at asymmetric sites on both sides of a 2D material. The potential differences between two Cr atom layers are 0.27 and 0.52 eV/ $\text{\AA}$  for 33.3% and 44.4% oxygen adsorbed structures, respectively as depicted in Figure 5a,b. Owing to the built-in electric field, the spin magnetic moment of atoms in the antiferromagnetic state will be reversed, and a certain net magnetic moment will be generated (0.35 and 0.07  $\mu\text{B}/\text{atom}$  for 33.3% and 44.4% adsorption states, respectively). Half-metal for 33.3% adsorption concentration (0.38 eV band gap for spin-up electrons) and semiconductor state for 44.4% adsorption concentration (direct band gap 0.21 eV) can be achieved with specific configuration shown in Figures 5c,d and S13, attributing to the existence of built-in electric field. In this way, we can control the band gap and the magnetic ground state by asymmetrical adsorption on both sides of monolayers, which is a new avenue to realize magnetic half-metals or semiconductors for spintronic devices.

## CONCLUSIONS

In conclusion, through the regulation of electronic localization and superexchange interaction by oxygen group functionalization, we have realized the control of electronic and magnetic ground states in MBene  $\text{Cr}_2\text{B}_2$ . With fully oxygen group termination,  $\text{Cr}_2\text{B}_2\text{O}_2$  exhibits antiferromagnetic semiconductor characteristics, whereas pristine  $\text{Cr}_2\text{B}_2$  is a ferromagnetic metal. The antiferromagnetism arises from interlayer superexchange interaction, while the intralayer interaction exhibits ferromagnetism. When applying strain, transition between different antiferromagnetic states is observed along with the transition from semiconductor to metal. The interlayer

superexchange interaction changes from AFM to FM, leading to the transformation of different antiferromagnetic orders. Furthermore, we first realize ferromagnetic semiconductor and ferromagnetic half-metallic states, originating from the built-in electric field introduced by nonuniform adsorption on both sides of the atomic layer. The antiferromagnetic semiconductor  $\text{Cr}_2\text{B}_2\text{O}_2$  with a tunable band gap and high Néel temperature (425 K) demonstrates the high potential for the utilization in innovative spintronics and electronic devices.

## ■ ASSOCIATED CONTENT

### SI Supporting Information

The Supporting Information is available free of charge at <https://pubs.acs.org/doi/10.1021/acs.jpcc.2c03909>.

Computational details, SOC effect on electronic structure, magnetic anisotropy energy, transition temperature, stress-strain curve, band evolution and structures with strain, normalized magnetism evolution with strain, nonuniform oxygen group adsorbed structures and band structures, table of energy magnetic exchange constants and electrical properties for different strains; and total energies for different oxygen concentration configurations ([PDF](#))

## ■ AUTHOR INFORMATION

### Corresponding Authors

Jian Zhou — School of Materials Science and Engineering, Beihang University, Beijing 100191, China; Center for Integrated Computational Materials Engineering, International Research Institute for Multidisciplinary Science, Beihang University, Beijing 100191, China; Email: [jzhou@buaa.edu.cn](mailto:jzhou@buaa.edu.cn)

Zhimei Sun — School of Materials Science and Engineering, Beihang University, Beijing 100191, China; Center for Integrated Computational Materials Engineering, International Research Institute for Multidisciplinary Science, Beihang University, Beijing 100191, China;  [orcid.org/0000-0002-4438-5032](https://orcid.org/0000-0002-4438-5032); Email: [zmsun@buaa.edu.cn](mailto:zmsun@buaa.edu.cn)

### Authors

Shucheng Xing — School of Materials Science and Engineering, Beihang University, Beijing 100191, China; Center for Integrated Computational Materials Engineering, International Research Institute for Multidisciplinary Science, Beihang University, Beijing 100191, China

Bikun Zhang — School of Materials Science and Engineering, Beihang University, Beijing 100191, China; Center for Integrated Computational Materials Engineering, International Research Institute for Multidisciplinary Science, Beihang University, Beijing 100191, China

Complete contact information is available at: <https://pubs.acs.org/doi/10.1021/acs.jpcc.2c03909>

### Notes

The authors declare no competing financial interest.

## ■ ACKNOWLEDGMENTS

This work was financially supported by the National Natural Science Foundation of China (Nos. 51871009 and 51872017). The authors thank the High-Performance Computing (HPC) resources of Beihang University.

## ■ REFERENCES

- Wolf, S. A.; Awschalom, D. D.; Buhrman, R. A.; Daughton, J. M.; von Molnár, S.; Roukes, M. L.; Chtchelkanova, A. Y.; Treger, D. M. Spintronics: A Spin-Based Electronics Vision for the Future. *Science* **2001**, *294*, 1488–1495.
- Baltz, V.; Manchon, A.; Tsoi, M.; Moriyama, T.; Ono, T.; Tserkovnyak, Y. Antiferromagnetic spintronics. *Rev. Mod. Phys.* **2018**, *90*, No. 015005.
- Mermin, N. D.; Wagner, H. Absence of Ferromagnetism or Antiferromagnetism in One- or Two-Dimensional Isotropic Heisenberg Models. *Phys. Rev. Lett.* **1966**, *17*, 1133–1136.
- Huang, B.; Clark, G.; Navarro-Moratalla, E.; Klein, D. R.; Cheng, R.; Seyler, K. L.; Zhong, D.; Schmidgall, E.; McGuire, M. A.; Cobden, D. H.; Yao, W.; Xiao, D.; Jarillo-Herrero, P.; Xu, X. Layer-dependent ferromagnetism in a van der Waals crystal down to the monolayer limit. *Nature* **2017**, *546*, 270–273.
- Gong, C.; Li, L.; Li, Z.; Ji, H.; Stern, A.; Xia, Y.; Cao, T.; Bao, W.; Wang, C.; Wang, Y.; Qiu, Z. Q.; Cava, R. J.; Louie, S. G.; Xia, J.; Zhang, X. Discovery of intrinsic ferromagnetism in two-dimensional van der Waals crystals. *Nature* **2017**, *546*, 265–269.
- Zhang, C.; Wang, X.; Mi, W. Sd transition-metal atom/5d–3d dimer adsorption tailored electronic structure and magnetic anisotropy of two-dimensional WSe<sub>2</sub> monolayers. *J. Mater. Chem. C* **2020**, *8*, 11417–11425.
- Song, C.; Xiao, W.; Li, L.; Lu, Y.; Jiang, P.; Li, C.; Chen, A.; Zhong, Z. Tunable band gap and enhanced ferromagnetism by surface adsorption in monolayer Cr<sub>2</sub>Ge<sub>2</sub>Te<sub>6</sub>. *Phys. Rev. B* **2019**, *99*, No. 214435.
- Frey, N. C.; Bandyopadhyay, A.; Kumar, H.; Anasori, B.; Gogotsi, Y.; Shenoy, V. B. Surface-Engineered MXenes: Electric Field Control of Magnetism and Enhanced Magnetic Anisotropy. *ACS Nano* **2019**, *13*, 2831–2839.
- Chaves, A.; Azadani, J. G.; Alsalmán, H.; da Costa, D. R.; Frisenda, R.; Chaves, A. J.; Song, S. H.; Kim, Y. D.; He, D.; Zhou, J.; Castellanos-Gómez, A.; Peeters, F. M.; Liu, Z.; Hinkle, C. L.; Oh, S.-H.; Ye, P. D.; Koester, S. J.; Lee, Y. H.; Avouris, P.; Wang, X.; Low, T. Bandgap engineering of two-dimensional semiconductor materials. *NPJ 2D Mater. Appl.* **2020**, *4*, No. 29.
- Cui, Q.; Liang, J.; Shao, Z.; Cui, P.; Yang, H. Strain-tunable ferromagnetism and chiral spin textures in two-dimensional Janus chromium dichalcogenides. *Phys. Rev. B* **2020**, *102*, No. 094425.
- Chittari, B. L.; Lee, D.; Banerjee, N.; MacDonald, A. H.; Hwang, E.; Jung, J. Carrier- and strain-tunable intrinsic magnetism in two-dimensional MAX<sub>3</sub> transition metal chalcogenides. *Phys. Rev. B* **2020**, *101*, No. 085415.
- Deng, Y.; Yu, Y.; Song, Y.; Zhang, J.; Wang, N. Z.; Sun, Z.; Yi, Y.; Wu, Y. Z.; Wu, S.; Zhu, J.; Wang, J.; Chen, X. H.; Zhang, Y. Gate-tunable room-temperature ferromagnetism in two-dimensional Fe<sub>3</sub>GeTe<sub>2</sub>. *Nature* **2018**, *563*, 94–99.
- Zhang, X. X.; Li, L.; Weber, D.; Goldberger, J.; Mak, K. F.; Shan, J. Gate-tunable spin waves in antiferromagnetic atomic bilayers. *Nat. Mater.* **2020**, *19*, 838–842.
- Sztenkiel, D.; Foltyń, M.; Mazur, G. P.; Adhikari, R.; Kosiel, K.; Gas, K.; Zgirski, M.; Kruszka, R.; Jakielka, R.; Li, T.; Piotrowska, A.; Bonanni, A.; Sawicki, M.; Dietl, T. Stretching magnetism with an electric field in a nitride semiconductor. *Nat. Commun.* **2016**, *7*, No. 13232.
- Law, J. Y.; Franco, V.; Moreno-Ramírez, L. M.; Conde, A.; Karpenkov, D. Y.; Radulov, I.; Skokov, K. P.; Gutfleisch, O. A quantitative criterion for determining the order of magnetic phase transitions using the magnetocaloric effect. *Nat. Commun.* **2018**, *9*, No. 2680.
- Seo, J.; De, C.; Ha, H.; Lee, J. E.; Park, S.; Park, J.; Skourski, Y.; Choi, E. S.; Kim, B.; Cho, G. Y.; Yeom, H. W.; Cheong, S.-W.; Kim, J. H.; Yang, B.-J.; Kim, K.; Kim, J. S. Colossal angular magnetoresistance in ferrimagnetic nodal-line semiconductors. *Nature* **2021**, *599*, 576–581.
- Bleibaum, O.; Belitz, D. Weak localization of electrons in an external electric field. *Phys. Rev. B* **2004**, *69*, No. 075119.

- (18) Tito, M. A.; Pusep, Y. A. Localized-to-extended-states transition below the Fermi level. *Phys. Rev. B* **2018**, *97*, No. 184203.
- (19) Herbschleb, E. D.; Kato, H.; Maruyama, Y.; Danjo, T.; Makino, T.; Yamasaki, S.; Ohki, I.; Hayashi, K.; Morishita, H.; Fujiwara, M.; Mizuochi, N. Ultra-long coherence times amongst room-temperature solid-state spins. *Nat. Commun.* **2019**, *10*, No. 3766.
- (20) Nair, R. S.; Barati, E.; Gupta, K.; Yuan, Z.; Kelly, P. J. Spin-Flip Diffusion Length in 5d Transition Metal Elements: A First-Principles Benchmark. *Phys. Rev. Lett.* **2021**, *126*, No. 196601.
- (21) Guo, L.; Yan, Y.; Xu, R.; Li, J.; Zeng, C. Zero-Bias Conductance Peaks Effectively Tuned by Gating-Controlled Rashba Spin-Orbit Coupling. *Phys. Rev. Lett.* **2021**, *126*, No. 057701.
- (22) Jiang, H.; Zheng, L.; Liu, Z.; Wang, X. Two-dimensional materials: From mechanical properties to flexible mechanical sensors. *InfoMat* **2020**, *2*, 1077–1094.
- (23) Akgenc, B.; Vatansever, E.; Ersan, F. Tuning of electronic structure, magnetic phase, and transition temperature in two-dimensional Cr-based Janus MXenes. *Phys. Rev. Mater.* **2021**, *5*, No. 083403.
- (24) Abdullahi, Y. Z.; Vatansever, Z. D.; Ersan, F.; Akinci, U.; Akturk, O. U.; Akturk, E. Ferromagnetic TM<sub>2</sub>BC (TM = Cr, Mn) monolayers for spintronic devices with high Curie temperature. *Phys. Chem. Chem. Phys.* **2021**, *23*, 6107–6115.
- (25) Abdullahi, Y. Z.; Ersan, F.; Vatansever, Z. D.; Akturk, E.; Akturk, O. Ü. Exploring the potential of MnX (S, Sb) monolayers for antiferromagnetic spintronics: A theoretical investigation. *J. Appl. Phys.* **2020**, *128*, No. 113903.
- (26) Abdullahi, Y. Z.; Ersan, F.; Akturk, E.; Akturk, O. U. Theoretical Screening of Metal Borocarbide Sheets for High-Capacity and High-Rate Li and Na-Ion Batteries. *Phys. Rev. Appl.* **2021**, *16*, No. 024031.
- (27) Guo, Z.; Zhou, J.; Sun, Z. New two-dimensional transition metal borides for Li ion batteries and electrocatalysis. *J. Mater. Chem. A* **2017**, *5*, 23530–23535.
- (28) Li, Y.; Li, L.; Huang, R.; Wen, Y. Computational screening of MBene monolayers with high electrocatalytic activity for the nitrogen reduction reaction. *Nanoscale* **2021**, *13*, 15002–15009.
- (29) Jia, J.; Li, B.; Duan, S.; Cui, Z.; Gao, H. Monolayer MBenes: prediction of anode materials for high-performance lithium/sodium ion batteries. *Nanoscale* **2019**, *11*, 20307–20314.
- (30) Zhang, T.; Zhang, B.; Peng, Q.; Zhou, J.; Sun, Z. Mo<sub>2</sub>B<sub>2</sub> MBene-supported single-atom catalysts as bifunctional HER/OER and OER/ORR electrocatalysts. *J. Mater. Chem. A* **2021**, *9*, 433–441.
- (31) Zhang, B.; Zhou, J.; Guo, Z.; Peng, Q.; Sun, Z. Two-dimensional chromium boride MBenes with high HER catalytic activity. *Appl. Surf. Sci.* **2020**, *500*, No. 144248.
- (32) Abdullahi, Y. Z.; Vatansever, Z. D.; Akturk, E.; Akinci, Ü.; Akturk, O. Ü. A tetragonal phase Mn<sub>2</sub>B<sub>2</sub> sheet: a stable room temperature ferromagnet with sizable magnetic anisotropy. *Phys. Chem. Chem. Phys.* **2020**, *22*, 10893–10899.
- (33) Jiang, Z.; Wang, P.; Jiang, X.; Zhao, J. MBene (MnB): a new type of 2D metallic ferromagnet with high Curie temperature. *Nanoscale Horiz.* **2018**, *3*, 335–341.
- (34) Abdullahi, Y. Z.; Vatansever, Z. D.; Akturk, E.; Akinci, Ü.; Akturk, O. Ü. Novel two-dimensional CrXB<sub>2</sub> (X=Cr, Ru) metal for high Néel temperature antiferromagnetic spintronics. *J. Solid State Chem.* **2021**, *302*, No. 122427.
- (35) Kresse, G.; Furthmüller, J. Efficiency of ab-initio total energy calculations for metals and semiconductors using a plane-wave basis set. *Comput. Mater. Sci.* **1996**, *6*, 15–50.
- (36) Kresse, G.; Joubert, D. From ultrasoft pseudopotentials to the projector augmented-wave method. *Phys. Rev. B* **1999**, *59*, 1758–1775.
- (37) Ade, M.; Hillebrecht, H. Ternary Borides Cr<sub>2</sub>AlB<sub>2</sub>, Cr<sub>3</sub>AlB<sub>4</sub>, and Cr<sub>4</sub>AlB<sub>6</sub>: The First Members of the Series (CrB<sub>2</sub>)<sub>n</sub>CrAl with n = 1, 2, 3 and a Unifying Concept for Ternary Borides as MAB-Phases. *Inorg. Chem.* **2015**, *54*, 6122–6135.
- (38) Wang, L.; Maxisch, T.; Ceder, G. Oxidation energies of transition metal oxides within the GGA + U framework. *Phys. Rev. B* **2006**, *73*, No. 195107.
- (39) Jain, A.; Hautier, G.; Ong, S. P.; Moore, C. J.; Fischer, C. C.; Persson, K. A.; Ceder, G. Formation enthalpies by mixing GGA and GGA + U calculations. *Phys. Rev. B* **2011**, *84*, No. 045115.
- (40) Togo, A.; Tanaka, I. First principles phonon calculations in materials science. *Scr. Mater.* **2015**, *108*, 1–5.
- (41) Heyd, J.; Scuseria, G. E.; Ernzerhof, M. Hybrid functionals based on a screened Coulomb potential. *J. Chem. Phys.* **2003**, *118*, 8207–8215.
- (42) Sorescu, D. C.; Lee, J.; Al-Saidi, W. A.; Jordan, K. D. Coadsorption properties of CO<sub>2</sub> and H<sub>2</sub>O on TiO<sub>2</sub> rutile (110): A dispersion-corrected DFT study. *J. Chem. Phys.* **2012**, *137*, No. 074704.
- (43) He, X.; Helbig, N.; Verstraete, M. J.; Bousquet, E. TB2J: A python package for computing magnetic interaction parameters. *Comput. Phys. Commun.* **2021**, *264*, No. 107938.
- (44) Boker, S.; Neale, M.; Maes, H.; Wilde, M.; Spiegel, M.; Brick, T.; Spies, J.; Estabrook, R.; Kenny, S.; Bates, T.; Mehta, P.; Fox, J. OpenMx: An Open Source Extended Structural Equation Modeling Framework. *Psychometrika* **2011**, *76*, 306–317.
- (45) Liechtenstein, A. I.; Katsnelson, M. I.; Antropov, V. P.; Gubanov, V. A. Local spin density functional approach to the theory of exchange interactions in ferromagnetic metals and alloys. *J. Magn. Magn. Mater.* **1987**, *67*, 65–74.
- (46) Evans, R. F. L.; Fan, W. J.; Chureemart, P.; Ostler, T. A.; Ellis, M. O. A.; Chantrell, R. W. Atomistic spin model simulations of magnetic nanomaterials. *J. Phys.: Condens. Matter* **2014**, *26*, No. 103202.
- (47) Nakamura, S.; Gohda, Y. Prediction of ferromagnetism in MnB and MnC on nonmagnetic transition-metal surfaces studied by first-principles calculations. *Phys. Rev. B* **2017**, *96*, No. 245416.
- (48) Zhang, H.; Xiang, H.; Dai, F.-z.; Zhang, Z.; Zhou, Y. First demonstration of possible two-dimensional MBene CrB derived from MAB phase Cr<sub>2</sub>AlB<sub>2</sub>. *J. Mater. Sci. Technol.* **2018**, *34*, 2022–2026.
- (49) Kan, D.; Wang, D.; Zhang, X.; Lian, R.; Xu, J.; Chen, G.; Wei, Y. Rational design of bifunctional ORR/OER catalysts based on Pt/Pd-doped Nb<sub>2</sub>CT<sub>2</sub> MXene by first-principles calculations. *J. Mater. Chem. A* **2020**, *8*, 3097–3108.
- (50) Jungwirth, T.; Sinova, J.; Manchon, A.; Marti, X.; Wunderlich, J.; Felser, C. The multiple directions of antiferromagnetic spintronics. *Nat. Phys.* **2018**, *14*, 200–203.
- (51) Anderson, P. W. Antiferromagnetism. Theory of Superexchange Interaction. *Phys. Rev.* **1950**, *79*, 350–356.
- (52) Kanamori, J. Superexchange interaction and symmetry properties of electron orbitals. *J. Phys. Chem. Solids* **1959**, *10*, 87–98.
- (53) Hu, J.; Wang, P.; Zhao, J.; Wu, R. Engineering magnetic anisotropy in two-dimensional magnetic materials. *Adv. Phys. X* **2018**, *3*, No. 1432415.
- (54) Daalderop, G. H. O.; Kelly, P. J.; Schuurmans, M. F. H. First-principles calculation of the magnetocrystalline anisotropy energy of iron, cobalt, and nickel. *Phys. Rev. B* **1990**, *41*, 11919–11937.
- (55) Zhang, Q.; Gao, Y.; Xu, Z.; Wang, S.; Kobayashi, H.; Wang, J. The Effects of Oxygen Functional Groups on Graphene Oxide on the Efficient Adsorption of Radioactive Iodine. *Materials* **2020**, *13*, No. 5770.